

# Preparation and characterization of Ce–Mn–O composites with applications in catalytic wet oxidation processes

G. Blanco,<sup>1\*</sup> M. A. Cauqui,<sup>1</sup> J. J. Delgado,<sup>1</sup> A. Galtayries,<sup>2</sup> J. A. Pérez-Omil<sup>1</sup> and J. M. Rodríguez-Izquierdo<sup>1</sup>

<sup>1</sup> Departamento de Ciencia de los Materiales e Ingeniería Metalúrgica y Química Inorgánica, Facultad de Ciencias, Universidad de Cádiz, Apartado 40, E-11510 Puerto Real (Cádiz), Spain

<sup>2</sup> Laboratoire de Physico-Chimie des Surfaces, Ecole Nationale Supérieure de Chimie de Paris, F-75231 Paris, France

Received 29 July 2003; Revised 28 November 2003; Accepted 1 December 2003

A series of Ce–Mn composites with different compositions was prepared by co-precipitation. All samples were characterized by x-ray diffraction (XRD), x-ray photoelectron spectroscopy (XPS), energy dispersive spectroscopy (EDS) and transmission electron microscopy (TEM). According to their size and chemical composition, two different kinds of particles were observed: (a) small crystallites of Ce–Mn solid solution (<7 nm), and (b) large particles of manganese oxides with different reduction degrees (>50 nm). These results were used to explain differences between the surface and bulk compositions of the samples as well as the specific surface area. Furthermore, from XPS studies, the presence of various Mn species with different oxidation states could be stated. This fact might clarify the exceptional catalytic behaviour of the samples for the catalytic wet oxidation of toxic organic compounds. Copyright © 2004 John Wiley & Sons, Ltd.

**KEYWORDS:** catalytic wet oxidation; Ce–Mn–O composites; XPS; TEM; EDS

## INTRODUCTION

The need for improved wastewater treatments, due to the restrictive environmental regulations and health quality standards that apply in developed countries, has increased during the past few years. Industrial effluent streams from many industrial processes contain high concentrations of toxic organic compounds. Nowadays, wet oxidation (WO) is an attractive method for the treatment of waste streams which are too dilute to be incinerated (100 g L<sup>-1</sup>) and yet too toxic to be biologically processed. In fact, there are more than 200 plants worldwide that use this technology.<sup>1,2</sup> Unfortunately, the efficient removal of pollutants requires excessive pressures (1–35 MPa), as well as high temperatures (200–400 °C).<sup>3</sup>

In order to decrease reaction times and to operate under less severe conditions in WO processes, many catalysts have been tested.<sup>1,3</sup> Homogeneous catalysts such as copper salts are amongst the most active catalysts, and are used in practical wastewater treatments.<sup>4,5</sup> However, recovery of the copper salts is necessary to prevent the contamination of water by toxic copper ions.<sup>1</sup> Because of this, heterogeneous

catalysts are preferred. In this sense, heterogeneous Ce–Mn composite oxide catalysts have proved to be powerful oxidation catalysts for organic pollutants.<sup>6–8</sup> In previous studies, Imamura *et al.* noticed that the composition of Mn–Ce catalysts exerts a strong effect on their catalytic activity.<sup>7,9,10</sup> However, despite the increasing number of studies in this direction, research is generally focused only on the redox properties of these materials. Therefore, the aim of this work is to make a structural and surface characterization of a series of Ce–Mn catalysts, with special interest on the nanostructure of the samples. This study can be useful in order to establish a connection between catalyst properties and catalytic activity.

## EXPERIMENTAL

Manganese and cerium composite oxides were prepared by co-precipitation from aqueous solutions of Mn(II) and Ce(III) nitrates (Merck) with the desired atomic ratios, followed by drying at 100 °C and calcination in air at 500 °C for 1 hour. Table 1 gives the chemical composition measured by inductively coupled plasma (ICP) analysis and the specific surface areas of the samples.

X-ray diffraction (XRD) analyses were performed on a Philips PW1820 diffractometer (Cu K<sub>α</sub> radiation) operating at 40 kV and 40 mA. Transmission electron microscopy (TEM) and energy dispersive spectroscopy (EDS) measurements were performed on a FEI CM200Feg microscope

\*Correspondence to: G. Blanco, Departamento de Ciencia de los Materiales e Ingeniería Metalúrgica y Química Inorgánica, Facultad de Ciencias, Universidad de Cádiz, Apartado 40, E-11510 Puerto Real (Cádiz), Spain. E-mail: ginesa.blanco@uca.es  
Contract/grant sponsor: Ministerio de Ciencia y Tecnología; Contract/grant numbers: AMB99-0791; MAT2002-02600.

with a structural resolution of 0.23 nm. The sample was ultrasonically suspended in hexane and deposited on a Cu grid recovered with a thin layer of carbon (holey carbon). A VG Escalab Mk II spectrometer equipped with non-monochromatic Mg  $K_{\alpha}$  and Al  $K_{\alpha}$  radiation was employed for the XPS experiments. The powders were stuck on a double-sided adhesive conducting polymer tape. Binding energy correction was done by using the C 1s core level at 284.9 eV as an internal reference.

## RESULTS AND DISCUSSION

XRD patterns of the Ce–Mn composites are shown in Fig. 1. The diffractogram corresponding to CM95 (i.e. Ce-rich sample, Fig. 1(d)) is characteristic of the fluorite-like  $\text{CeO}_2$  structure (JCPDS 43–1002). No other crystalline phases, nor amorphous phases, were detected in this sample, either by XRD or by HREM, so all Mn cations should be incorporated into the  $\text{CeO}_2$  lattice, as a Ce–Mn solid solution. On the other hand, all peaks of pure Mn oxide pattern (Fig. 1(a)) can be attributed to  $\alpha\text{-Mn}_2\text{O}_3$  (JCPDS 24-0508). A mixture of both phases, as well as other Mn oxides, was observed for intermediate compositions, CM15 and CM50, as in Figs 1(b) and (c), respectively. It is difficult to unequivocally identify these new oxide phases because of the similarity between the XRD patterns of many Mn oxides. Nevertheless, the presence of  $\text{Mn}_5\text{O}_8$  (JCPDS 39–1218) and  $\beta\text{-MnO}_2$  (JCPDS 44–0141) has been established by HREM.<sup>11</sup> Thus, addition

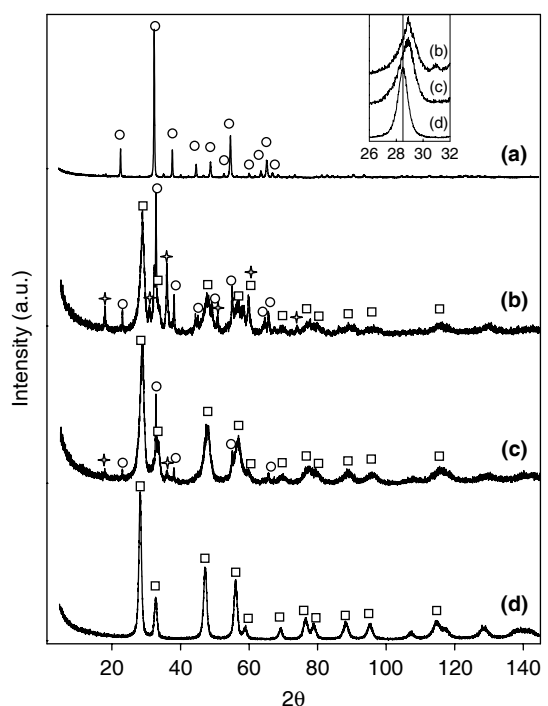


**Figure 1.** Powder XRD diffractograms of Ce–Mn composites with different compositions: (a) CM0; (b) CM15; (c) CM50; and (d) CM95. The reference patterns for  $\alpha\text{-Mn}_2\text{O}_3$  (○) and  $\text{CeO}_2$  fluorite (□) are shown, as well as peaks that can be attributed to  $\text{Mn}_5\text{O}_8$  or  $\beta\text{-MnO}_2$  (+). The inset shows the shift on the fluorite (111) peak to lower angles when the Ce content of the samples increases.

of Ce seemed to stabilize Mn oxide species with oxidation states higher than (III).

This strong segregation of phases was confirmed by TEM and EDS data. Figure 2 shows a typical TEM image of a sample with an intermediate composition. According to their size and chemical composition, two different kinds of particles could be distinguished. The first type of crystallites (A-type) consists of large particles (>50 nm) of cerium-free Mn oxides, as shown by EDS analysis. The second type of particles (B-type crystallites) consists of small crystals (<7 nm) of a Ce–Mn solid solution. EDS analysis of these B-type crystallites showed that the Mn content on this phase (column 6 of Table 1) increases with the total Mn content of the sample. The low solubility limit of Mn in the ceria lattice observed in this work (max. 20 mol.%), is in agreement with the relatively large difference between Shannon radii of  $\text{Ce}^{4+}$  (101.2 pm) and  $\text{Mn}^{2+}$  (79.5 pm) or  $\text{Mn}^{3+}$  (72 pm). In this sense, progressive shift of XRD peaks corresponding to the fluorite-like phase towards higher Bragg angles is in good agreement with the incorporation of the small Mn cations into the ceria lattice, causing the contraction of its unit cell. Finally as far as the EDS study is concerned, no evidence of pure ceria phase has been detected.

The surface area of the sample decreases as the Mn content in the samples increases (Table 1). This is related to the formation of the large A-type particles of  $\text{MnO}_x$ . In fact, the sample with the highest surface area is CM95 ( $77.1 \text{ m}^2 \text{ g}^{-1}$ ), the one with only B-type crystals of Ce–Mn solid solution. On the other hand, pure Mn oxide (CM0), where only A-type crystallites were found, showed the lowest surface area ( $9.0 \text{ m}^2 \text{ g}^{-1}$ ). Obviously, the contribution to the surface of small B-type crystallites is more significant than that of the large A-type particles.

XPS spectra of the samples were obtained by using an Al  $K_{\alpha}$  source, except for the particular study of the Ce 3d core level carried out to measure the Ce oxidation state. In this latter case, a Mg  $K_{\alpha}$  source was used, in order to avoid Auger peaks corresponding to Mn which appear inside the Ce 3d area.

Columns 7 to 10 of Table 1 summarize the results from the XPS analysis of the set of samples. Columns 7 and 8

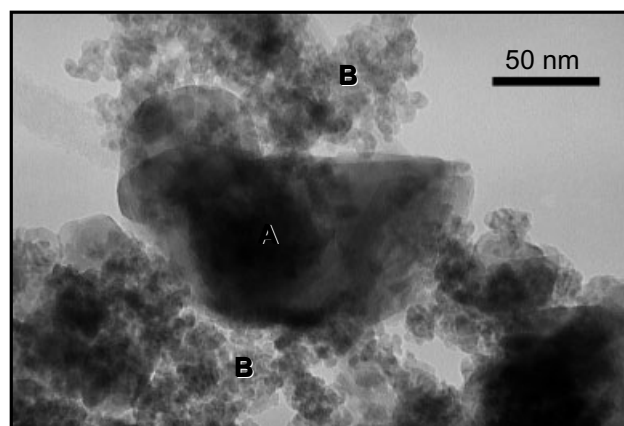


**Figure 2.** TEM experimental image of CM50 sample showing the A- and B-type crystallites referred to in the text. Local chemical composition was determined by EDS.

**Table 1.** Quantitative data from the analysis of the Ce–Mn composites

Sample	$S_{\text{BET}}$ ( $\text{m}^2 \cdot \text{g}^{-1}$ )	ICP		EDS		XPS		BE (eV)	
		% Ce	% Mn	% Ce	% Mn	% Ce	% Mn	O 1s	$\frac{\text{Mn } 2p_{3/2}}{A}$
CM15	77.1	14.8	85.2	80	20	39	61	529.4	641.6
CM50	69.3	42.7	57.3	85	15	62	38	529.4	641.3
CM95	37.3	93.5	6.5	94	6	93	7	528.9	640.9
CM0	9.0	0	100	–	–	–	–	–	–

in the table show surface Ce and Mn molar percentages, as obtained by integration of the corresponding Ce 3d and Mn 2p spectra, respectively. It is evident from the data reported, that a surface enrichment in Ce has occurred, similar to that reported by Chen *et al.*<sup>12</sup> These authors attribute the Ce surface enrichment to the coverage of the Mn crystals by a thin layer of a Ce-rich oxide phase. However, our data can be explained on the basis of the nanostructure observed by both HREM and XRD data. Thus, the low Mn surface content can be related to the size of A-type Mn oxide crystallites, their contribution to the total surface area of the sample being significantly smaller than that of the small Ce-rich B-type crystallites.

The O 1s spectra were also recorded, although they are not shown. All the spectra showed two main features: one broad peak at high BE ( $\sim 532$  eV) attributed to adsorbed species ( $\text{H}_2\text{O}$ ,  $\text{CO}_2$ , surface OH species), and a second narrower peak, that can be attributed to lattice oxygen. The O 1s binding energies for this second peak are reported in column 9 of Table 1. Thus, for CM15 and CM50, the composites with the highest Mn content, the position of the peak can be related to Mn oxides,<sup>13</sup> whereas for CM95, where only mixed Ce/Mn phase was observed, the position of the peak is close to that reported for ceria-based mixed oxides (528.8 eV).<sup>14</sup>

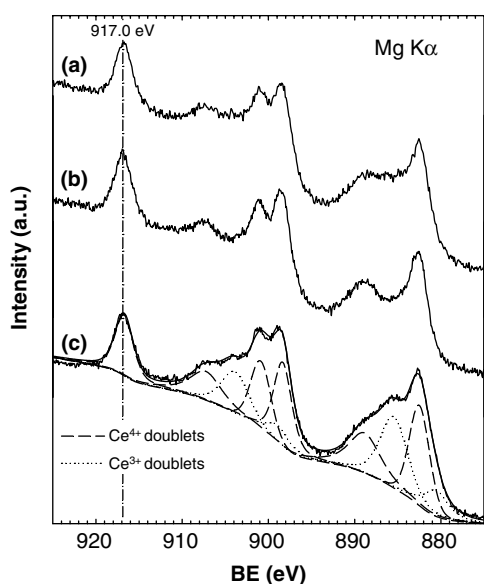


**Figure 3.** XPS spectra corresponding to Ce 3d core levels of (a) CM15, (b) CM50 and (c) CM95. This latter spectrum has been deconvoluted in order to distinguish Ce(IV) and Ce(III) contributions.

Further analysis was performed on Ce 3d and Mn 2p core levels (Figs 3 and 4). The position of the lower kinetic energy peak for Ce 3d (917.0 eV) was not shifted with respect to the one reported for pure  $\text{CeO}_2$  in the literature.<sup>15</sup> The spectra have been deconvoluted to calculate the Ce(III) contribution. For the highest Mn loadings (CM15 and CM50), the Ce(III) content of the samples was almost negligible. However, a significant increase of the reduction degree of Ce was observed for the Ce-rich sample (CM95). Peak decomposition of the spectrum (Fig. 3(c)) allowed us to calculate Ce(III) content as being ca. 34%. Likewise, the Mn reduction degree changes with the chemical composition of the samples. Figure 4 accounts for Mn 2p spectra of the composites. The main Mn  $2p_{3/2}$  component is denoted as A in the figure, and a shift to lower binding energies from CM15 (curve (a)) to CM95 (curve (c)) could be observed. The position of this peak is also shown in Table 1. The Mn 2p spectrum for CM95 also shows a second feature, denoted as B in Fig. 4, that is attributed to a satellite structure for Mn(II).<sup>16</sup> The peaks noted as A can be attributed to Mn in low oxidation states,

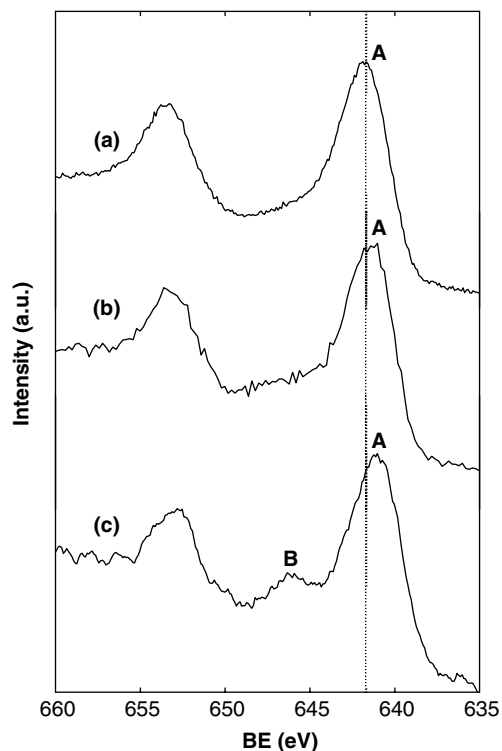


**Figure 4.** XPS spectra corresponding to Mn 2p core levels of (a) CM15, (b) CM50 and (c) CM95. Refer to Table 1 for positions of A and B features.

Mn(III) or Mn(II). The progressive shift to lower binding energies can be attributed to a lowering of the oxidation state of Mn from Mn(III) to Mn(II), as the relative importance of solid solution B-type crystallites increases. Therefore, for samples with higher Mn content, Mn(III) is the predominant oxidation state, whereas for lower Mn loadings the trivalent oxidation state becomes less significant in favour of lower (2+) oxidation states. The existence of various oxidation states can facilitate electron transfer processes during the radical production step in the catalytic wet oxidation of organic pollutants.<sup>12</sup>

## CONCLUSIONS

X-ray powder diffraction characterization of Ce–Mn composites indicates a cubic solid solution for high Ce contents and a  $\alpha$ -Mn<sub>2</sub>O<sub>3</sub> structure for pure Mn oxide. In the case of intermediate compositions, a mixture of both structures was observed, as well as highly oxidized Mn phases (Mn<sub>5</sub>O<sub>8</sub> and  $\beta$ -MnO<sub>2</sub>). Thus, Ce seems to stabilize Mn oxides with high oxidation state. In this sense, XPS studies revealed the presence of Mn species with different oxidation states that can contribute to the activity of catalysts in CWO processes. The surface area loss and the surface enrichment in Ce observed with increasing Mn contents are attributed to the formation of large Mn oxide particles (A-type particles).

## Acknowledgements

This work has been supported by the Ministerio de Ciencia y Tecnología (Projects AMB99-0791 and MAT2002-02600).

## REFERENCES

1. Matatov-Meytal YI, Sheintuch M. *Ind. Eng. Chem. Res.* 1998; **37**: 309.
2. Luck F. *Catal. Today* 1999; **53**: 81.
3. Mishra VS, Mahajani VV, Joshi JB. *Ind. Eng. Chem. Res.* 1995; **34**: 2.
4. Tagashira Y, Takagi K, Inagaki K. Japan Patent number 75 106 862, 1976.
5. Shende RV, Mahajani VV, Vijaykumar V. *Ind. Eng. Chem. Res.* 1997; **36**: 4809.
6. Hamoudi S, Larachi F, Sayari A. *J. Catal.* 1998; **177**: 247.
7. Imamura S, Nakamura M, Kawabata N, Yoshida J. *Ind. Eng. Chem. Prod. Res. Dev.* 1986; **25**: 34.
8. Hamoudi S, Belkacemi K, Larachi F. *Chem. Eng. Sci.* 1999; **54**: 3569.
9. Imamura S, Doi A, Ishida S. *Ind. Eng. Chem. Prod. Res. Dev.* 1985; **24**: 75.
10. Imamura S, Okumura Y, Nishio T, Utani K, Matsumura Y. *Ind. Eng. Chem. Res.* 1998; **37**: 1136.
11. Delgado JJ, PhD Thesis, University of Cadiz, 2003.
12. Chen H, Sayari A, Adnot A, Larachi F. *Appl. Catal. B.* 2001; **32**: 195.
13. Stochmeier BR, Hercules DM. *J. Phys. Chem.* 1984; **88**: 4922.
14. Galtayries A, Blanco G, Cifredo GA, Finol D, Gatica JM, Pintado JM, Vidal H, Sporken R, Bernal S. *Surf. Interface Anal.* 1999; **27**: 941.
15. Laachir A, Perrichon V, Badri A, Lamotte J, Catherine E, Lavalley JC, el Fallah J, Hilaire L, le Normand F, Quémère E, Sauvion GN, Touret O. *J. Chem. Soc. Faraday Trans.* 1991; **87**: 1601.
16. Mirabella F, Johnson RL, Ghijsen J. *Surf. Sci.* 2002; **506**: 172.